

## Prediction of a Dirac state in monolayer $\text{TiB}_2$

L. Z. Zhang,<sup>1,2</sup> Z. F. Wang,<sup>2</sup> S. X. Du,<sup>1,\*</sup> H.-J. Gao,<sup>1</sup> and Feng Liu<sup>2,3,\*</sup>

<sup>1</sup>*Institute of Physics, Chinese Academy of Sciences, Beijing 100190, China*

<sup>2</sup>*Department of Materials Science and Engineering, University of Utah, Salt Lake City, Utah 84112, USA*

<sup>3</sup>*Collaborative Innovation Center of Quantum Matter, Beijing 100871, China*

(Received 22 August 2014; revised manuscript received 19 September 2014; published 3 October 2014)

We predict the existence of a Dirac state in a monolayer  $\text{TiB}_2$  sheet ( $m\text{-TiB}_2$ ), a two-dimensional metal diboride, based on first-principles calculations. The band structure of  $m\text{-TiB}_2$  is found to be characterized with anisotropic Dirac cones with the largest Fermi velocity of  $0.57 \times 10^6$  m/s, which is about one-half of that of graphene. The Dirac point is located at the Fermi level between the  $K$  and  $\Gamma$  points, with the Dirac states arising primarily from the  $d$  orbitals of Ti. Freestanding  $m\text{-TiB}_2$  exhibits a bending instability, so that a planar  $m\text{-TiB}_2$  needs to be stabilized on a substrate. The calculation of  $m\text{-TiB}_2$  on a  $h\text{-BN}$  substrate reveals a negligible influence of the  $h\text{-BN}$  substrate on the electronic properties of  $m\text{-TiB}_2$ . Our findings extend the Dirac materials to metal diborides.

DOI: [10.1103/PhysRevB.90.161402](https://doi.org/10.1103/PhysRevB.90.161402)

PACS number(s): 61.46.–w, 68.55.–a, 73.22.–f

Graphene, due to its special two equivalent carbon sublattices in the honeycomb structure, has massless carriers which can be described by Dirac equations and are called Dirac fermions [1]. Such Dirac materials, with a linear band dispersion around the Fermi level, display ballistic charge transport and an enormously high carrier mobility [1]. Since Dirac fermions were first observed in graphene [1–3], Dirac states have been proposed and studied in many other Dirac materials. These include molecular graphene [4], janugraphene and chlorographene [5],  $\alpha$ - and  $\beta$ -graphyne [6], strongly bound graphene/intercalated transition metal/SiC(0001) ( $G/i\text{-TM/SiC}$ ) [7], the surface of topological insulators [8], silicene and germanene [9],  $Pmmn$  boron [10], and two-dimensional (2D) organic topological insulators [11]. The search for Dirac materials has been ongoing. Especially, it is interesting to go beyond the carbonic and topological materials.

Boron, as the neighbor of carbon in the periodic table, has attracted enormous interest for the past few years [10,12,13]. Due to its open electron shell structure (one electron short of being half filled), B can easily bind with transition metal atoms. Up to now, many metal-boron nanostructures have been predicted, including nanotubes [14–17] and nanosheets [18–20]. Especially in a planar metal-diboride structure, such as  $\text{BeB}_2$ , B atoms form a hexagonal lattice such as graphene and Be atoms provide the missing valence electrons. As such, the charge arrangements in the B layer are very similar to graphene, suggesting a high structural stability [17]. This metal doping mechanism can be extended to other metal-diboride systems, whose electronic properties can be turned by using different metals [18–20]. Experimentally, the formation of multilayer  $\text{MgB}_2$  sheets on a  $\text{Mg}(0001)$  surface [21] and multilayer  $\text{TiB}_2$  sheets at the interface of  $\text{TiC}$  and  $\text{B}_4\text{C}$  have been reported [22].

In this Rapid Communication, we investigate the electronic properties and stability of monolayer  $\text{TiB}_2$  sheets ( $m\text{-TiB}_2$ ) by using first-principles calculations. We find that  $m\text{-TiB}_2$  turns out to be a Dirac material, exhibits Dirac cones near the Fermi level ( $E_F$ ), and is characterized with a Fermi velocity that is about one-half of that of graphene. Different from the  $p$ -orbital

Dirac state in graphene, the Dirac states in  $m\text{-TiB}_2$  are of a  $d$ -orbital character, arising predominantly from the  $d$  orbitals of Ti. The Dirac points are located at off-symmetry points in between  $K$  and  $\Gamma$ . Importantly, we point out that freestanding  $m\text{-TiB}_2$  exhibits a bending instability so that a planar  $m\text{-TiB}_2$  needs to be stabilized on a substrate. Calculation of  $m\text{-TiB}_2$  on a  $h\text{-BN}$  substrate shows that the Dirac states are retained on the  $h\text{-BN}$  substrate.

All density functional theory (DFT) calculations are carried by using the Vienna *ab initio* simulation package (VASP) [23,24] with the projector augmented wave method [25]. The local density approximation [26] in the form of Perdew-Zunger [27] is adopted for the exchange-correlation function. The energy cutoff of the plane-wave basis sets is 400 eV. The Monkhorst-Pack scheme with  $27 \times 27 \times 1$   $k$  points is used to sample the Brillouin zone. For the model containing  $4 \times 4$   $m\text{-TiB}_2$  on  $5 \times 5$   $h\text{-BN}$ , a  $9 \times 9 \times 1$   $k$ -point sampling is used, and the whole  $h\text{-BN}$  substrate is fixed. For calculations of the  $\text{TiB}_2$  nanotubes, the  $1 \times 1 \times 27$   $k$ -point sampling is used. In all the calculations, a 15 Å vacuum layer is used and all atoms are fully relaxed in geometric optimizations until the residual forces on each atom are smaller than 0.01 eV/Å. The phonon frequencies are calculated by using a supercell approach as implemented in the PHONOPY code [28,29].

Figure 1(a) shows the top and side views of the optimized structures of  $m\text{-TiB}_2$  in a presumed planar structure. One unit cell contains two B atoms and one Ti atom. B atoms are arranged in a honeycomb lattice, and Ti atoms are located in the middle of the hexagons. This monolayer sheet can be considered as a one layer cutting from the bulk  $\text{TiB}_2$  or the Ti adsorbed graphenelike B sheet. The B-B bond length  $l_{\text{B-B}}$  is 1.79 Å, which is about the same as in the bulk  $\text{TiB}_2$  (1.73 Å), but slightly larger than that of the B sheet (1.67 Å) [13,30]. The vertical distance between the Ti and B layer is 1.19 Å, which is noticeably smaller than that in the bulk  $\text{TiB}_2$  (1.575 Å), indicating a much stronger interaction between the Ti atoms and B layer. The binding energy between the Ti and B layer is found to be  $E_b = -9.17$  eV/unit cell ( $E_b = E_{\text{tot}} - E_{h\text{-BS}} - E_{\text{Ti}}$ ). We calculated the formation energy ( $\Delta E$ ) per  $\text{TiB}_2$  unit of  $m\text{-TiB}_2$  relative to the  $\text{TiB}_2$  nanotubes. The  $\text{TiB}_2$  nanotubes tend to bend towards the B

\*Corresponding authors: [sxdu@iphy.ac.cn](mailto:sxdu@iphy.ac.cn); [fliu@eng.utah.edu](mailto:fliu@eng.utah.edu)

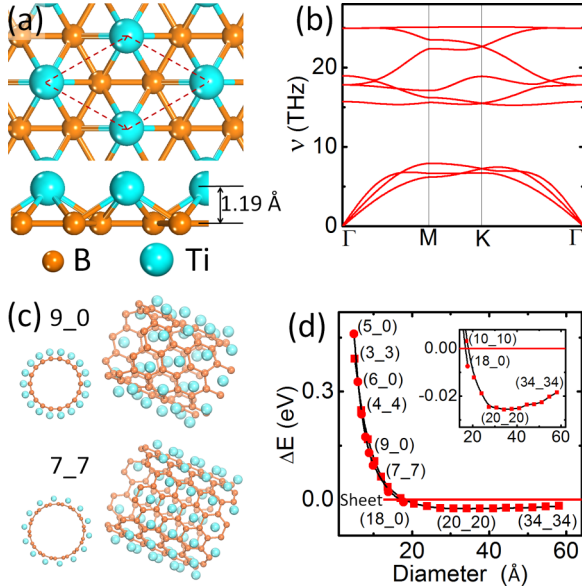


FIG. 1. (Color online) (a) Top and side views of  $m$ -TiB<sub>2</sub>. (b) The phonon-dispersion curves of  $m$ -TiB<sub>2</sub>. (c) Schematic structures for TiB<sub>2</sub> zigzag (9<sub>0</sub>) and armchair (7<sub>7</sub>) nanotubes. (d) Relative formation energies vs the diameters of TiB<sub>2</sub> nanotubes (red dots/squares corresponding to zigzag/armchair nanotubes), where the formation energy per TiB<sub>2</sub> unit cell is measured with respect to the  $m$ -TiB<sub>2</sub> (red line). The inset shows the zoom-in of (d).

side, as shown in Fig. 1(c). Figure 1(d) shows that  $m$ -TiB<sub>2</sub> is more stable than small nanotubes with a diameter less than that of the (18,0) tube, but less stable than other larger ones. This indicates a bending instability of planar  $m$ -TiB<sub>2</sub> into a tubular shape, an interesting point we will discuss further later on. On the other hand, we also calculated phonon-dispersion curves of  $m$ -TiB<sub>2</sub>, as shown in Fig. 1(b). The absence of imaginary frequencies demonstrates the dynamical stability of  $m$ -TiB<sub>2</sub>.

The calculated band structures and projected density of states (PDOS) of  $m$ -TiB<sub>2</sub> are shown in Fig. 2(a). The main feature of the band structure is two linear bands crossing at the  $E_F$  and located at an off-symmetry  $D$  [(0.143, 0.286) \*  $2\pi/a$ ] point, between the  $K$  and  $\Gamma$  points ( $\sim 0.43\Gamma-K$ ). The PDOS shows that the Dirac states near the  $E_F$  are predominantly contributed by Ti. We also plot the three-dimensional (3D) valence and conduction bands in Fig. 2(b), which clearly show the anisotropy of the Dirac cone. The right panel of Fig. 2(b) shows the constant-energy contour for the valence band around one Dirac cone with an energy interval of 0.1 eV. The oval-shaped contour lines indicate that this Dirac cone is anisotropic with the largest Fermi velocity of  $0.57 \times 10^6$  m/s, and the linear dispersion maintains about  $\pm 0.3$  eV away from the Dirac point. Both the Fermi velocity and the energy range of the Dirac state are close to one-half of those in freestanding graphene [31]. We also checked by including spin-orbital coupling, which causes a small spin splitting of bands, but without inducing a gap (see Fig. S4 in the Supplemental Material [32]).

To understand the origin of the Ti orbital-originated Dirac states, the band structures of a triangular Ti lattice (at the same lattice constants as in  $m$ -TiB<sub>2</sub>) are calculated [blue

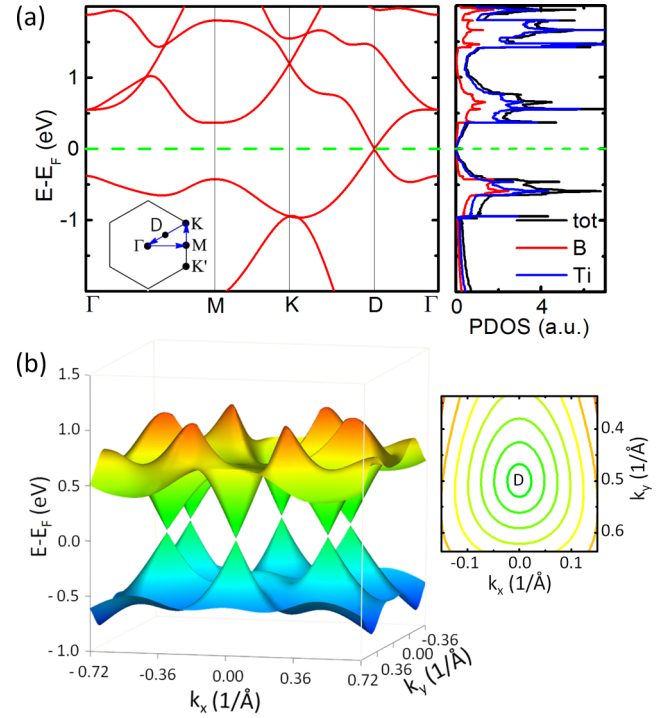


FIG. 2. (Color online) Electronic structures of  $m$ -TiB<sub>2</sub>. (a) Band structure and PDOS. (b) 3D valence and conduction bands and the Dirac cone in the vicinity of the Dirac point. The right panel of (b) shows the constant-energy contour for the valence band around one Dirac cone with an energy contour interval of 0.1 eV.

line in Fig. 3(a)]. Because of the  $D_{6h}$  symmetry, the Ti  $3d$  orbitals split into  $e_1(d_{xy}, d_{x^2-y^2})$ ,  $e_1^*(d_{xz}, d_{yz})$ , and  $a_1^*(d_{z^2})$  in the triangular lattice. Correspondingly, the band structures show five energy levels along the  $K$  point: two couples of degenerate level  $e_1$  and  $e_1^*$  and one  $a_1^*$ . By using the WANNIER90 package [33], we fit a tight-binding (TB) Hamiltonian with

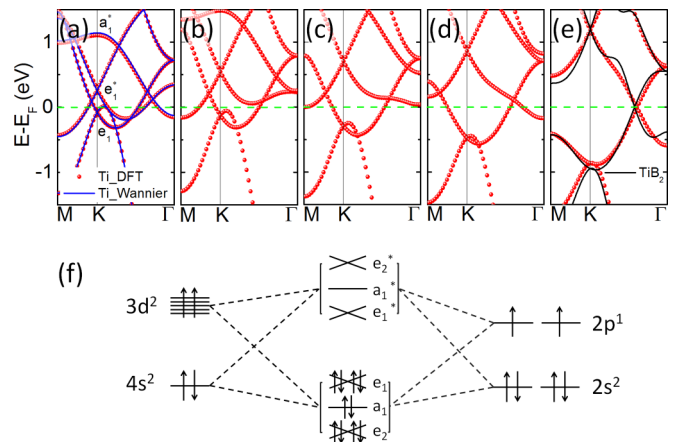


FIG. 3. (Color online) (a) First-principles and Wannier band structures for triangular Ti. (e) Band structures for triangular Ti at the appropriate on-site energy (red points) and  $m$ -TiB<sub>2</sub> (black line). (b)–(d) Band structures at 20%, 40%, and 60% on-site energy rectifications of that in (e). (f) Schematic drawing of the orbital hybridization between Ti and B. Each arrow denotes one electron with an up or down spin.

TABLE I. On-site energy rectifications for different orbitals in Fig. 3(e) compared with that in Fig. 3(a).

$s$	$p_z$	$p_x$	$p_y$	$d_{z^2}$	$d_{xz}$	$d_{yz}$	$d_{x^2-y^2}$	$d_{xy}$
-1.3	-1.05	-2	-2	1.6	0.8	0.8	-0.2	-0.2

maximally localized Wannier functions to the bands calculated by the first-principles method [red dots in Fig. 3(a)]. They show very good agreement. Then, we artificially tuned the on-site energies of the nine orbitals in the TB model (shown in Table I) to reveal how the band structure of the triangular Ti lattice would evolve [Figs. 3(b)–3(d)] until, with a chosen set of parameters, it [red dots in Fig. 3(e)] would match closely with the band structure of  $m$ -TiB<sub>2</sub> [black line in Fig. 3(e)] around the Fermi level. This allows us to qualitatively confirm that the off-symmetry Dirac states come mainly from the Ti  $d$  orbitals. [7] The calculated projected band structures (Fig. 4) also show that the bands near the Fermi level are mainly contributed by the Ti  $d$  orbitals. From Figs. 3(b)–3(d), where 20%, 40%, and 60% of the on-site energy rectifications are taken in comparison with Fig. 3(e), respectively, we see that the Dirac bands arise from band splitting around the Fermi level. Because  $m$ -TiB<sub>2</sub> has  $C_{6v}$  symmetry, Ti  $3d$  orbitals have a similar splitting mode as that of triangular Ti (the same energy sequence). As the triangular Ti lattice interacts with the hexagonal B lattice in  $m$ -TiB<sub>2</sub>, the B crystal field increases the band splitting of the Ti lattice. Specifically, the effect of the B lattice on the  $d$  orbitals of Ti is strongest in the  $z$  direction. Consequently, the change of the on-site energies of the  $d_{xz}$ ,  $d_{yz}$ , and  $d_{z^2}$  orbitals with  $z$  components is much larger than those of the  $d_{xy}$  and  $d_{x^2-y^2}$  orbitals without  $z$  components (Table I).

Figure 3(f) schematically shows the hybridization between Ti and B. The interaction between the Ti sublattice and B sublattice leads to ten hybridized states,  $e_2$ ,  $a_1$ ,  $e_1$ ,  $e_1^*$ ,  $a_1^*$ , and  $e_2^*$ , respectively.  $e_1$ ,  $e_1^*$ , and  $a_1^*$  come from the triangular Ti sublattice [Fig. 5(a)], and  $e_2$ ,  $a_1$ , and  $e_2^*$  come from the  $sp^2$  hybridizations in the B sublattice [Fig. 5(b)] [34];  $e_2$  and  $a_1$  consist of  $s$ ,  $p_x$ , and  $p_y$  characters ( $\sigma$  bands) of B, and  $e_1$  and  $e_1^*$  consist of  $d$  orbitals of Ti. Ten electrons, four from Ti and six from B, fully occupy the  $e_2$ ,  $a_1$ , and  $e_1$  states, leaving the five states with high energy empty. Thus, the interactions between

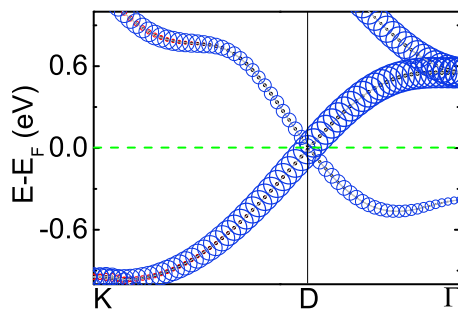


FIG. 4. (Color online) Projected band structures of  $m$ -TiB<sub>2</sub> near the Dirac point, where the radii of the blue (red, black) circles are proportional to the Ti  $d$  (B  $p_z$ , B  $s + p_x + p_y$ ) character.

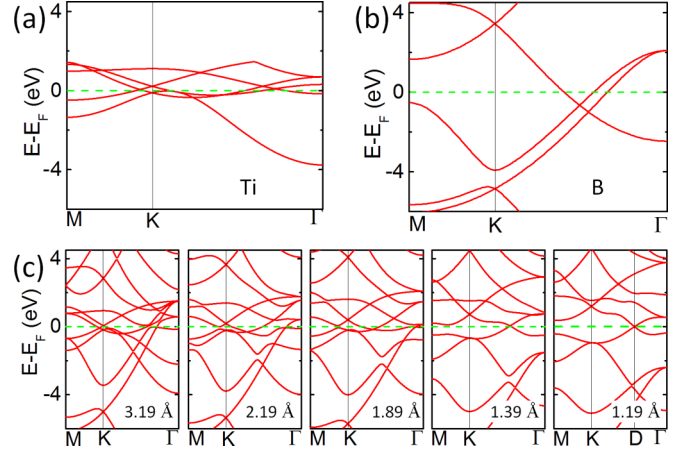


FIG. 5. (Color online) Band structures of (a) the triangular Ti, (b) hexagonal boron, and (c)  $m$ -TiB<sub>2</sub> at different distances from the Ti and boron layer (from 3.19 to 1.19 Å).

the Ti  $d$  orbitals and B  $p$  orbitals result in the appearance of a Dirac point at the  $D$  point [Fig. 5(c)].

Most theoretically predicted and experimentally confirmed Dirac materials, such as graphene and topological insulators, are composed of  $p$ -orbital electrons. Within the single-particle band picture, there is no difference between the  $d$ -orbital and  $p$ -orbital linear Dirac band dispersions [35,36]. However, generally the  $d$ -orbital Dirac materials have a stronger spin exchange interaction, a larger spin-orbit coupling, and a more significant many-body correlation effect, which may yield new and rich physics, such as the anomalous quantum Hall effect [37], Mott insulator [38], etc. Therefore, the prediction of different  $d$ -orbital Dirac materials is of both scientific and technological interest. Specifically, the  $d$ -orbital Dirac state predicted in the  $m$ -TiB<sub>2</sub> has several interesting features: (1) It has a highly anisotropic Dirac band structures [right part in Fig. 2(b)], which is desirable for manipulating the direction of electron propagation [39,40]. (2) It has a large Fermi velocity, which is comparable to the largest value obtained in the graphene.

For most TiB<sub>2</sub> nanotubes [with diameters larger than that of the (18,0) tube] are more stable than  $m$ -TiB<sub>2</sub> [Fig. 1(b)], and the planar  $m$ -TiB<sub>2</sub> will bend into a tubular shape. Thus, a planar  $m$ -TiB<sub>2</sub> needs to be stabilized on a substrate to overcome its bending moment [41]. Here, we use the  $h$ -BN as the substrate, for two important reasons: (1) An infinite  $m$ -TiB<sub>2</sub> sheet or a wide enough  $m$ -TiB<sub>2</sub> nanoribbon can be

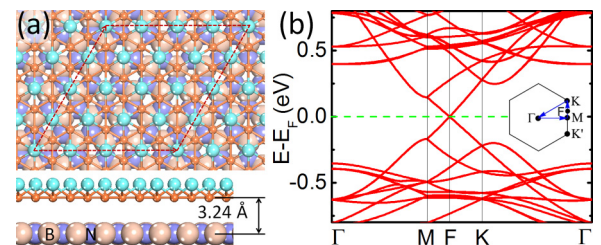


FIG. 6. (Color online) (a) Relaxed structures and (b) band structures of  $m$ -TiB<sub>2</sub> on  $h$ -BN.

stabilized on a *h*-BN substrate without bending. Based on stress calculations and following the analysis of Ref. [41], we estimated that the minimum width of a *m*-TiB<sub>2</sub> nanoribbon to be stabilized is 3.22 nm (see the Supplemental Material [32]). (2) The weak influence on the electronic properties of *m*-TiB<sub>2</sub>, which can retain the Dirac states of *m*-TiB<sub>2</sub>: According to the lattice constants of the *h*-BN and *m*-TiB<sub>2</sub>, we choose a model which contains  $4 \times 4$  *m*-TiB<sub>2</sub> on  $5 \times 5$  *h*-BN, and fix the lattice of the *h*-BN. This model closely approximates the real system, since the lattice mismatch between *m*-TiB<sub>2</sub> and the *h*-BN substrate is only 0.46%. The relaxed configuration of the *m*-TiB<sub>2</sub>/*h*-BN system is shown in Fig. 6(a). We find that the distance between *m*-TiB<sub>2</sub> and the *h*-BN substrate is about 3.24 Å, and the adsorption energy is 94 meV/TiB<sub>2</sub>. We also checked those results considering the van der Waals interactions. The resulting distance and adsorption energy is 3.08 Å and 435 meV/TiB<sub>2</sub>. However, band structures remain the same, [32] suggesting a weak interaction between *m*-TiB<sub>2</sub> and the substrate. Figure 6(b) shows the band structure of the *m*-TiB<sub>2</sub>/*h*-BN system. The linear dispersion relationship retains at the Dirac point. When *m*-TiB<sub>2</sub> is placed on the *h*-BN substrate, the periodicity is expanded into a  $4 \times 4$  supercell for *m*-TiB<sub>2</sub> (see Fig. S3 in the Supplemental Material [32]).

Consequently, the Dirac point moves to the *F* point in between *M* and *K* ( $\sim 0.44M-K$ ), which is folded from the *D* point of the *m*-TiB<sub>2</sub> band [Fig. 2(a)]. Thus, we confirm that the Dirac states of *m*-TiB<sub>2</sub> can be retained on the *h*-BN substrate.

In conclusion, by using first-principles calculations, *m*-TiB<sub>2</sub> is demonstrated to be a Dirac material which is energetically and dynamically stable. Different from graphene, the Dirac cone is anisotropic with the largest Fermi velocity of  $0.57 \times 10^6$  m/s, and has the characteristics of a transition metal *d* orbital. Further investigations show that the existence of *d*-band Dirac cones could be attributed to the *d*-band splitting of the triangular Ti layers. Calculation of *m*-TiB<sub>2</sub> on a *h*-BN substrate shows that the Dirac states are retained. Our study reveals a different kind of Dirac material—metal boride.

We thank Q. B. Yan, M. Zhou, and F. Ye for helpful discussions. This work was partially supported by the Natural Science Foundation of China (No. 51325204, No. 61390501 and No. 51210003), the MOST 973 projects of China (No. 2011CB921702), and the Chinese Academy of Sciences (CAS), Shanghai Supercomputer Center. Z.F.W and F.L. acknowledge support from DOE-BES (Grant No. DE-FG02-04ER46148).

- 
- [1] A. H. Castro Neto, N. M. R. Peres, K. S. Novoselov, and A. K. Geim, *Rev. Mod. Phys.* **81**, 109 (2012).
- [2] K. S. Novoselov, A. K. Geim, S. V. Morozov, D. Jiang, M. I. Katsnelson, I. V. Grigorieva, S. V. Dubonos, and A. A. Firsov, *Nature (London)* **438**, 197 (2005).
- [3] A. K. Geim and K. S. Novoselov, *Nat. Mater.* **6**, 183 (2007).
- [4] K. K. Gomes, W. Mar, W. Ko, F. Guinea, and H. C. Manoharan, *Nature (London)* **483**, 306 (2012).
- [5] Y. D. Ma, Y. Dai, and B. B. Huang, *J. Phys. Chem. Lett.* **4**, 2471 (2013).
- [6] D. Malko, C. Neiss, F. Viñes, and A. Görling, *Phys. Rev. Lett.* **108**, 086804 (2012).
- [7] Y. C. Li, P. C. Chen, G. Zhou, J. Li, J. Wu, B. L. Gu, S. B. Zhang, and W. H. Duan, *Phys. Rev. Lett.* **109**, 206802 (2012).
- [8] H. J. Zhang, C. X. Liu, X. L. Qi, X. Dai, Z. Fang, and S. C. Zhang, *Nat. Phys.* **5**, 438 (2009).
- [9] S. Cahangirov, M. Topsakal, E. Aktürk, H. Şahin, and S. Ciraci, *Phys. Rev. Lett.* **102**, 236804 (2009).
- [10] X. F. Zhou, X. Dong, A. R. Oganov, Q. Zhu, Y. J. Tian, and H. T. Wang, *Phys. Rev. Lett.* **112**, 085502 (2014).
- [11] Z. F. Wang, Z. Liu, and F. Liu, *Nat. Commun.* **4**, 1471 (2013).
- [12] N. Gonzalez Szwacki, A. Sadrzadeh, and B. I. Yakobson, *Phys. Rev. Lett.* **98**, 166804 (2007).
- [13] H. Tang and S. Ismail-Beigi, *Phys. Rev. Lett.* **99**, 115501 (2007).
- [14] S. Meng, E. Kaxiras, and Z. Y. Zhang, *Nano Lett.* **7**, 663 (2007).
- [15] A. Quandt, A. Y. Liu, and I. Boustani, *Phys. Rev. B* **64**, 125422 (2001).
- [16] S. Guerini and P. Piquini, *Microelectron. J.* **34**, 495 (2003).
- [17] V. V. Ivanovskaya, A. N. Enjashin, A. A. Sofronov, Y. N. Makurin, N. I. Medvedeva, and A. L. Ivanovskii, *J. Mol. Struct.: THEOCHEM* **625**, 9 (2003).
- [18] P. H. Zhang and V. H. Crespi, *Phys. Rev. Lett.* **89**, 056403 (2002).
- [19] H. Tang and S. Ismail-Beigi, *Phys. Rev. B* **80**, 134113 (2009).
- [20] S. Y. Xie, X. B. Li, W. Q. Tian, N. K. Chen, X. L. Zhang, Y. L. Wang, S. B. Zhang, and H. B. Sun, *Phys. Rev. B* **90**, 035447 (2014).
- [21] C. Cepek, R. Macovez, M. San Corti, L. Prtaccia, R. Larciprete, S. Lizzit, and A. Goldoni, *Appl. Phys. Lett.* **85**, 976 (2004).
- [22] G. Hilz and H. Holleck, *Int. J. Refract. Met. Hard Mater.* **14**, 97 (1996).
- [23] D. Vanderbilt, *Phys. Rev. B* **41**, 7892 (1990).
- [24] G. Kresse and J. Furthmüller, *Phys. Rev. B* **54**, 11169 (1996).
- [25] P. E. Blöchl, *Phys. Rev. B* **50**, 17953 (1994).
- [26] D. M. Ceperley and B. J. Alder, *Phys. Rev. Lett.* **45**, 566 (1980).
- [27] J. P. Perdew and A. Zunger, *Phys. Rev. B* **23**, 5048 (1981).
- [28] K. Parlinski, Z.-Q. Li, and Y. Kawazoe, *Phys. Rev. Lett.* **78**, 4063 (1997).
- [29] A. Togo, F. Oba, and I. Tanaka, *Phys. Rev. B* **78**, 134106 (2008).
- [30] X. B. Yang, Y. Ding, and J. Ni, *Phys. Rev. B* **77**, 041402(R) (2008).
- [31] P. R. Wallace, *Phys. Rev.* **71**, 622 (1947).
- [32] See Supplemental Material at <http://link.aps.org/supplemental/10.1103/PhysRevB.90.161402> for calculation details about the minimum width of the *m*-TiB<sub>2</sub> nanoribbon on *h*-BN, the calculation results of the *m*-TiB<sub>2</sub>/*h*-BN system by using the DFT+D/PBE method, the band folding from  $1 \times 1m$ -TiB<sub>2</sub> to  $4 \times 4m$ -TiB<sub>2</sub>, and the band structures of *m*-TiB<sub>2</sub> with spin-orbital coupling.
- [33] A. A. Mostofi, J. R. Yates, Y.-S. Lee, I. Souza, D. Vanderbilt, and N. Marzari, *Comput. Phys. Commun.* **178**, 685 (2008).
- [34] L. Z. Zhang, Q. B. Yan, S. X. Du, G. Su, and H. J. Gao, *J. Phys. Chem. C* **116**, 18202 (2012).
- [35] Z. Liu, Z. F. Wang, J. W. Mei, Y. S. Wu, and F. Liu, *Phys. Rev. Lett.* **110**, 106804 (2013).
- [36] M. Zhou, W. Ming, Z. Liu, Z. F. Wang, P. Li, and F. Liu, *Proc. Natl. Acad. Sci. USA*, doi:10.1073/pnas.1409701111.

- [37] Z. F. Wang, Z. Liu, and F. Liu, *Phys. Rev. Lett.* **110**, 196801 (2013).
- [38] I. I. Mazin, H. O. Jeschke, F. Lechermann, H. Lee, M. Fink, R. Thomale, and R. Valenti, *Nat. Commun.* **5**, 4261 (2014).
- [39] C. H. Park, L. Yang, Y. W. Son, M. L. Cohen, and S. G. Louie, *Nat. Phys.* **4**, 213 (2008).
- [40] Z. F. Wang and F. Liu, *ACS Nano* **4**, 2459 (2010).
- [41] D. C. Yu and F. Liu, *Nano Lett.* **7**, 3046 (2007).